Origin of the Surface Magnetic Dead Layer in Rare-Earth Titanates

Raphaël Aeschlimann, Manuel Bibes, Alexandre Gloter

ADVANCED MATERIALS INTERFACES
Open Access
www.advmatinterfaces.de

Origin of the Surface Magnetic Dead Layer in Rare-Earth Titanates

*Raphaël Aeschlimann, Manuel Bibes, and Alexandre Gloter**

Perovskite rare-earth titanates $RTiO_3$ display a rich array of magnetic and electronic properties, with a Mott-insulating ground state and ferro- or antiferromagnetic spin orders depending on the rare-earth R. The nominal Ti valence is 3+ with a corresponding $3d^1$ configuration. Yet, at the surface of both bulk and thin films of $RTiO_3$, the Ti valence has been found to strongly deviate towards the more stable 4+ state, adversely affecting magnetic properties. While this finding is rather ubiquitous, its exact origin is still poorly understood, which hampers the integration of $RTiO_3$ into complex heterostructures harnessing their rich physics. Here, scanning transmission electron microscope and electron energy loss spectroscopy experiments are used to analyze the top part of an epitaxial $DyTiO_3$ thin film displaying a well-developed Ti^{4+}-rich layer over several nanometres. It shows that this valence evolution is related to a combination of short-range ordered interstitial oxygen planes and Ti-Dy cationic imbalance. Both defects synergistically contribute to enough hole doping for a complete transition toward Ti^{4+} over a few unit-cells from the surface while a structure primarily of the perovskite-type is maintained.

1. Introduction

Since their first syntheses in bulk,[1–3] perovskite rare-earth titanates $RTiO_3$ (RTO) have been investigated to characterize and understand their peculiar electronic and magnetic properties. RTO compounds are Mott insulators[4,5] in which the valence and conduction bands are formed by Ti t_{2g} levels split by the orthorhombic crystal fields and thus have both a *d*-like character.[6,7] The Ti cations have a nominal 3+ valence with a spin S = 1/2 which orders antiferromagnetically for large rare-earths (La-Sm) and ferromagnetically with smaller rare-earths (Gd-Lu).[8–10] Hole doping (through R substitution by Ca or Sr) yields a transition to a metallic state with interesting physics (heavy fermion behavior, phase separation, etc.).[11–13]

Since the 3+ valence of Ti is unstable compared to 4+, at the surface of RTO samples exposed to the atmosphere the Ti valence is systematically found to deviate strongly toward 4+. This has been observed by X-ray absorption spectroscopy (XAS), X-ray photoelectron spectroscopy (XPS), or scanning transmission electron microscope and electron energy loss spectroscopy (STEM-EELS) in multiple compounds from the RTO family (see e.g.).[14–17] This may even occur in ultra-high vacuum, to the point that this apparent overoxidation of the Ti may seem unavoidable.[18] Specific capping layers can restore partly or fully the 3+ valence.[18,19] Yet, the difficulty to preserve the nominal Ti^{3+} state may thwart efforts to assemble RTO layers into heterostructures and thus craft novel phenomena arising from correlations, charge/spin/orbital reconstruction, and inversion symmetry breaking.[20–22] Surprisingly though, the mechanism underpinning this valence change at the surface of RTO compounds is still unclear. In this article, STEM-EELS is used to examine in detail the surface of $DyTiO_3$ (DTO) epitaxial thin films in which a few-nanometre-thick Ti^{4+}-rich layer was previously detected by XAS and XPS. This layer behaves as a paramagnetic dead layer (with uncoupled Dy^{3+} ions) degrading the macroscopic ferrimagnetic response of the film,[19] which exemplifies the need to gain more insight into the actual nature of the layer at the atomic scale.

Indeed, the bulk $DyTiO_3$ exhibits a noncollinear magnetic order with canted Dy moments, whose magnetization is antiferromagnetically coupled to the Ti spins, resulting in a saturation moment of 3.7 μB per formula unit. Additionally, this ferrimagnetic order has a Curie temperature of 60 K. The surface dead layer consists of areas where magnetic Ti^{3+} ions are substituted by nonmagnetic Ti^{4+} ions, as clearly shown by X-ray absorption spectroscopy (XAS).[19] Hysteresis measurements at the XAS Dy M_5 and Ti L_3 edges reveal that the presence of surface Ti^{4+} ions disrupts the interaction among the Dy^{3+} ions, thereby unleashing their strong paramagnetic behavior. While such cationic

R. Aeschlimann, M. Bibes
Laboratoire Albert Fert – CNRS, Thales
Université Paris-Saclay
Palaiseau 91120, France
A. Gloter
Laboratoire de Physique des Solides
CNRS
Université Paris-Saclay
Orsay 91400, France
E-mail: alexandre.gloter@universite-paris-saclay.fr

The ORCID identification number(s) for the author(s) of this article can be found under https://doi.org/10.1002/admi.202400489

DOI: 10.1002/admi.202400489

charge evolution near the surface establishes a comprehensive scenario for the transition from a bulk ferrimagnetic to a strong paramagnetic surface response,[19] it requires an almost complete change in the Ti valence over a few nanometers close to the surface while maintaining the overall perovskite structure. This is an intriguing situation, as a strong valence change is expected to occur along with structural reorganization. Oxygen reincoporation might easily occur close to the surface but additional structural features would be expected for a complete reoxidation and a $DyTiO_{3.5}$ stoichiometry. Furthermore, the surface is also expected to introduce an electrostatic potential discontinuity, prone to rearrange the charge spatial distribution. High angle annular dark field–scanning transmission electron microscope (HAADF-STEM) and STEM-EELS measurements have thus been employed to determine the structural, cationic, and anionic arrangement at the dead layer and have been compared with the Ti^{4+} concentration measured simultaneously and with first principle calculations of defective $DyTiO_3$ structures.

2. Results and Discussion

High-angle annular dark field–scanning transmission electron microscope (HAADF-STEM) images of the LAO-DTO-Pt layers are visible in **Figure 1**a. At low magnification, the HAADF images along with diffractograms (Figure 1b,c) evidence that the DTO thin film grows with orientation domains. DTO crystallizes in an orthorhombic unit cell with a Pnma space group (a_{DTO} = 5.681 Å, b_{DTO} = 7.655 Å, c_{DTO} = 5.355 Å),[3] that results in pseudocubic parameters (pc) of b_{pc} = 3.827 Å and a_{pc} = c_{pc} = 3.904 Å. The substrate LAO is a rhombohedral distorted perovskite with a pseudocubic lattice parameter of 3.787 Å at room temperature, causing a compressive strain to the DTO thin film. In order to minimize the strain, the b-axis of DTO lies within the thin-film layer plane, consistent with the two observed orientations as evidenced by the diffractograms D1 (zone axis $[101]_{DTO}$) and D2 (zone axis $[010]_{DTO}$). The bright field (BF) and medium angle annular dark field (MAADF)-STEM images measured simultaneously with the HAADF near the top of the DTO layers are visible in Figure 1d,e. A striking difference is the strong white areas extending typically 5 nm from the surface, only visible in the MAADF images, which typically indicates the presence of defects, disorder, or strain. Figure 1f exhibits an enlargement of the MAADF with HAADF images superimposed in its center. The overall perovskite crystallinity of the DTO is maintained as observed in the HAADF but it goes along with the presence of defects in this top part as evidenced by the MAADF contrast.

STEM-EELS experiments were done in order to quantify the valence of Ti and typical results are visible in **Figure 2**. The left part of the figure (Figure 2a–c) corresponds to EELS obtained with a monochromation of ca. 100 meV and a spatial resolution of typically 0.5 nm. The spectrum extracted at the position P3, located far from the interface, exhibits all the fine structures corresponding to a Ti^{3+}. It notably resembles to the one measured by X-ray absorption spectroscopy (XAS) using depth-sensitive X-ray Excited Optical Luminescence (XEOL) detection on DTO layers, that was showing a qualitative match to a multiplet calculation for a pure $3d^1$ ground state.[19] The spectrum measured at position P1, near the top surface, exhibits a strong crystal-field split of the L_3 and L_2 white lines that is typical for a primary Ti^{4+} component.

When compared to the spectrum measured by XAS in a similar DTO thin film by surface sensitive total electron yield (TEY) mode that was quantified to about 20% of residual Ti^{3+} (**Figure 3** of ref.[19]), the EELS spectrum P1 exhibits even less Ti^{3+}. It is, for instance, noticeable from the clearer splitting of the L_2 component. The exact residual Ti^{3+} component is difficult to assess, since the XAS or EELS Ti-L fine structure of a $3d^0$ grounds state will depend on the crystal field geometry and strength or to the presence of defects. For instance, the L_3-t_{2g} line of a cubic $SrTiO_3$ (STO) is extremely energetically thin and its maximum intensity is above the L_3-e_g when measured by XAS or EELS with energy resolution below 100 meV.[24,25] But with such energy resolution, even in the case of cubic STO, small spectral variation of the Ti-$L_{2,3,}$ like an edge blurring, can be observed for picometer scale variation of the unit cell as obtained by a mere temperature change.[26] Furthermore, many Ti-L edges measured for pure Ti^{4+} compound do not have as clear Ti-L splitting as for STO. It can be observed for non-cubic perovskites $PbTiO_3$,[27] and $BaTiO_3$,[28] or for pyrochlores $Eu_{2-x}Fe_xTi_2O_7$[29] and $Yb_2Ti_{2-x}Fe_xO_{7-d}$.[30] It is then difficult to assess the exact content of remaining Ti^{3+} without an adequate reference of the Ti^{4+} expected at the top of the DTO layer. The spectrum images have then been fitted by choosing the spectra from P1 and P3 as end-member components and the respective weights can be seen in Figure 2b. The weight of the component P1 exhibits a small plateau over 1.5 nm from the top interface, and then decreases down to zero at about 5–6 nm from the interface. Additional EELS experiments have been done without monochromation (energy resolution of about ca. 0.5 eV) but with a spatial resolution close to 0.1 nm. Results can be seen in Figure 2d–f. Spectra from the top part of the thin film (P4) and from the inside of the DTO layers (P5) exhibit clear differences, but the fine structures are less visible than in P1 and P3. On the other hand, the higher spatial resolution points more clearly to a plateau extending over ≈1.5 nm followed by a decay over ca. 3 more nanometres. Combining both types of STEM-EELS experiments and the discussion on the valence uncertainty to determine the residual Ti^{3+}, the plateau area corresponds to a Ti valence at least 90% tetravalent and possibly to an almost pure Ti^{4+}, explaining the saturation of valence values. A decay to a pure Ti^{3+} of bulk-like $DyTiO_3$ is then observed after ca. 3 nm more.

Two main crystallographic structures can harbor a large amount of Ti^{4+} in the context of such titanates. The first one is a $Dy_2Ti_2O_7$ pyrochlore and the second belongs to $[110]_{pc}$ layered perovskites (LP) $A_nB_nO_{(3n+2)}$, where $Dy_2Ti_2O_7$ constitutes the n = 4 member.[31] Figure 3 shows a higher magnification of STEM images for defects present at the top of the DTO thin film. As mentioned before, a cubic perovskite-type contrast is observed up to the surface of the film, and it excludes the possibility of a $Dy_2Ti_2O_7$ pyrochlore structure. It is also consistent with X-ray diffraction measurements on same samples exhibiting only DTO and LAO reflections.[17] On the other hand, defective lines are observed, notably along $\{110\}_{pc}$ directions and sometimes along $(001)_{pc}$, quite often starting at a distance of ca. 5 nm from the surface. In the case of the $\{110\}_{pc}$ type defect, it is extending somehow to the surface. In between these defect lines, typical areas of ca. 5 × 5 nm with higher crystallinity are present. The lattice continuity starting from the DTO interior part to the top part of the perovskite is sometimes not maintained when crossing through the defective areas. An anti-correlation of

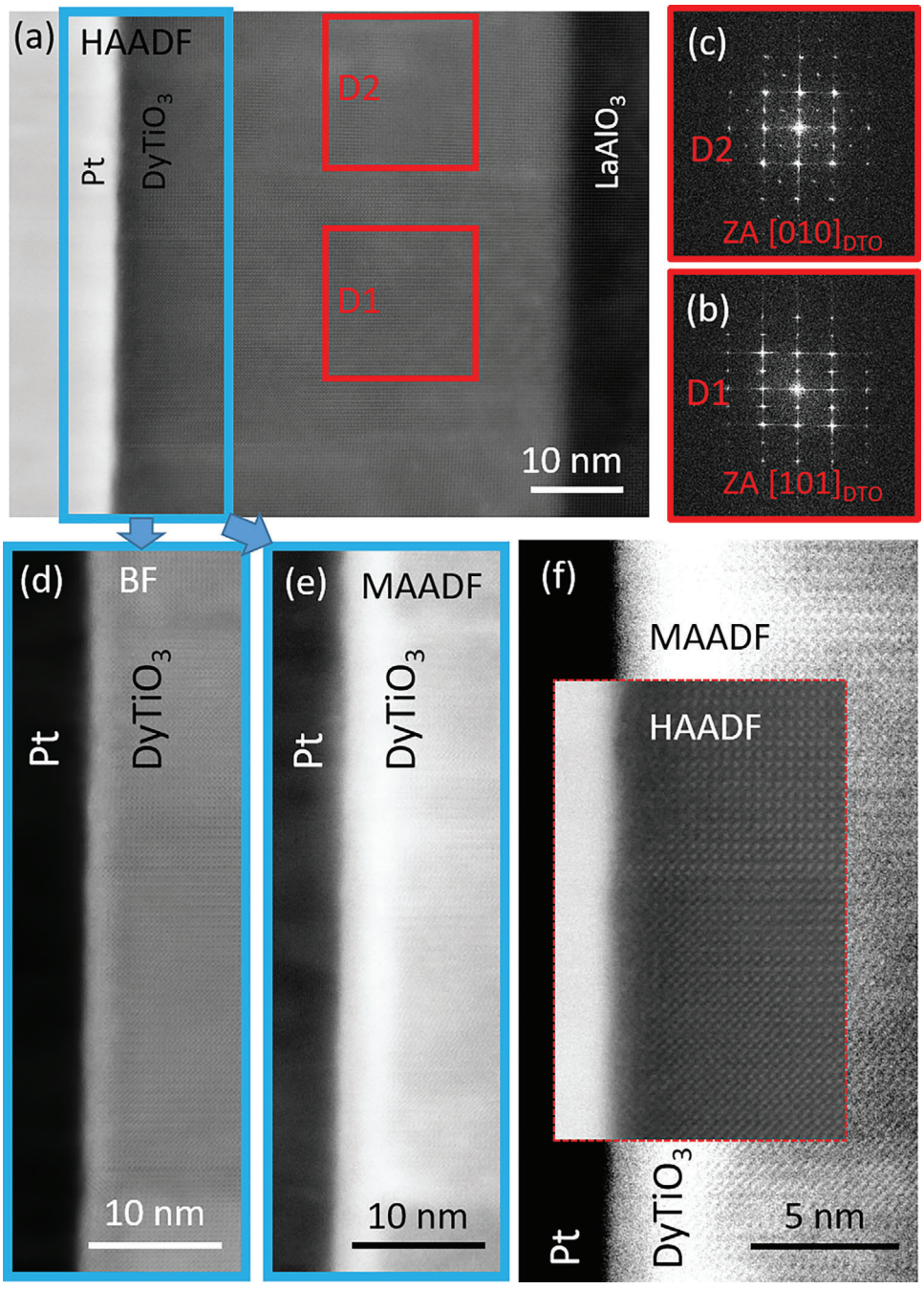

Figure 1. a–c) STEM-HAADF image of the $Pt/DyTiO_3/LaAlO_3$ heterostructure along with two diffractograms corresponding to orientation domains (red boxes D1 or D2) of the DTO. d,e) BF and MAADF STEM images corresponding to the blue boxed area of the HAADF image in (a). f) An HAADF inset is superimposed to an MAADF image showing that the white contrasted areas in MAADF coincide with a crystalline DTO structure as seen by HAADF.

the A and B sites indicates well-developed Ruddlesden–Popper (RP) type defects along the $(001)_{pc}$ planes as one can observe in Figure 3c. Such observations of RP defects are not so common. The most observed defects are along $\{110\}_{pc}$ planes and small phase shifts of the lattice can also be observed across these defects. It is more comparable to what would be expected for the insertion of interstitial oxygen (O_i) planes as in the case of $[110]_{pc}$ LP $Dy_2Ti_2O_7$. Excess oxygen atoms in these $\{110\}_{pc}$ planes have indeed been suggested as a mechanism for the oxidation of top DTO samples, but being randomly distributed[18] in contrast with the ordered LP $Dy_2Ti_2O_7$ cases. In the rare earth sequence, the LP $R_2Ti_2O_7$ phase is stable for the early R elements, with a threshold for R = Sm or Eu.[32] LP $La_2Ti_2O_7$ structures were, for instance, reported by TEM for ceramics[33] and by STEM in the case of films.[34] The stabilization of metastable LP $Dy_2Ti_2O_7$ was only recently obtained in films constrained by

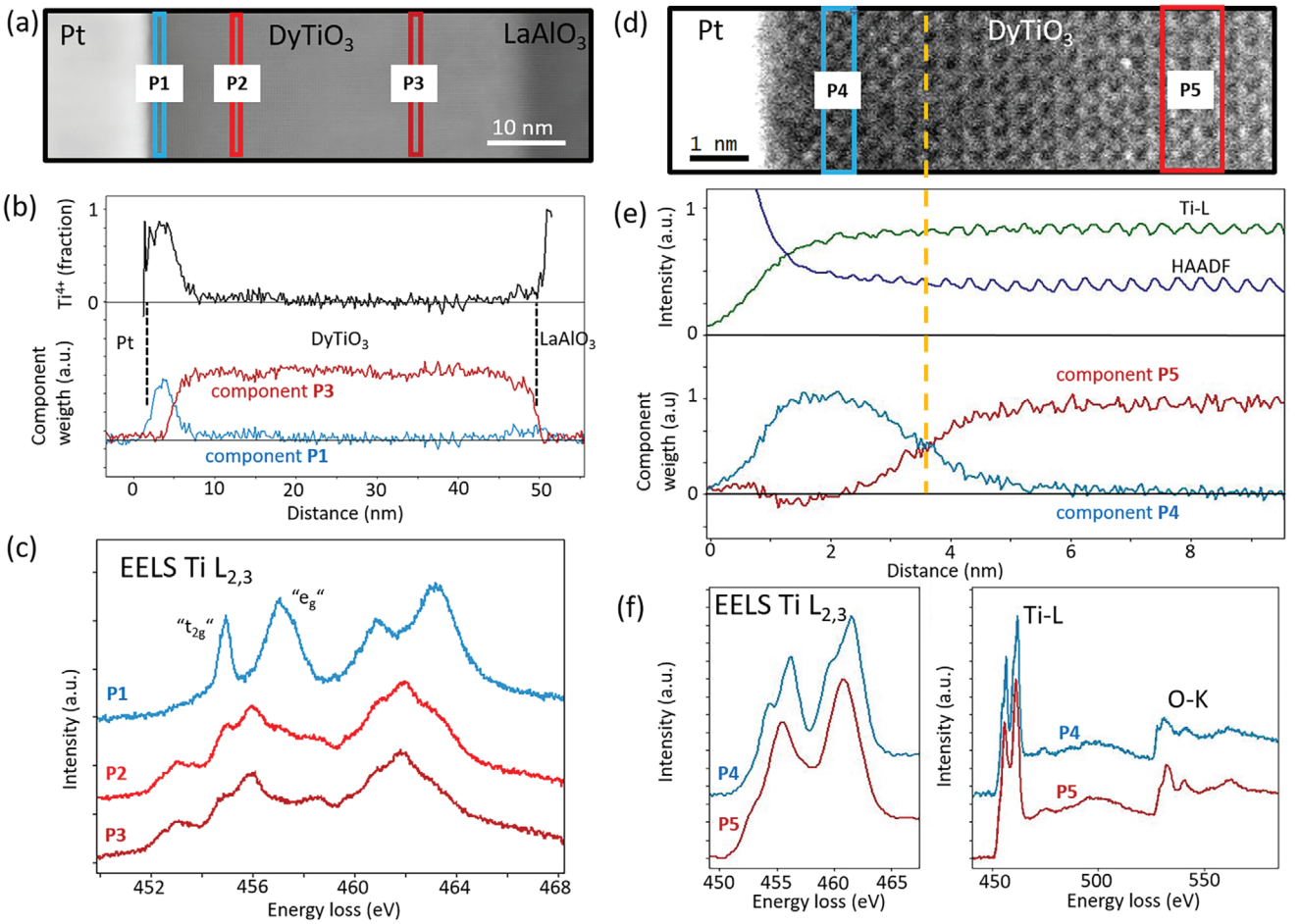

Figure 2. a–c) Monochromatic STEM-EELS at lower spatial resolution as seen in the HAADF images in (a). The spectra at (c) exhibit well-energetically resolved fine structures that can be assumed as almost pure Ti^{3+} for P3 and above 90% of Ti^{4+} in P1. The so-called "t_{2g}" and "e_g" lines have been noted for the L_3 line of the Ti^{4+} fine structure. The profiles obtained for the fitting weights of components P1 and P3 along with a typical Ti^{4+} fraction are shown in (b). d–f) Non-monochromatic STEM-EELS at higher spatial resolution as seen in the HAADF images in (d). Typical spectra of top (P4) and middle (P5) part of the DTO are in (f). Profiles of the fitting weights along with HAADF and Ti-L intensities are in (e).

an LP $La_2Ti_2O_7$ substrate and, the LP $Dy_2Ti_2O_7$ was then mostly observed near the interface.[31] It is then not surprising that long-range ordered planes of interstitial oxygens such as those present in LP $Dy_2Ti_2O_7$ were not observed. Here, only contrast on shorter length scales along $\{110\}_{pc}$ is observed and the periodicity of ca. 5 nm among these defects planes is very different from the case of LP $Dy_2Ti_2O_7$ where interstitial oxygen planes are spaced by 1.3 nm. Since the observed valence by EELS reveals a strong Ti^{4+} contribution, other defects might add up to produce this valence change.

EELS was performed across the film to quantify the chemical composition over an energy range large enough to pick up plasmon losses, Dy-N, O-K, Ti-L, and Dy-M edges (Figure S1, Supporting Information). The typical chemical composition across the whole DTO layer as measured by EELS for maps and profiles is displayed in **Figure** 4a,b. In the top area of the films, it is systematically observed an oxygen enrichment and a Ti/Dy ratio lower than 1 (cf. Figure 4b). Oxygen enrichment was expected from the $\{110\}_{pc}$ type defect and cationic misbalance can occur, e.g., from RP defects. Chemical maps have also been done near defects, see an example in Figure 4d,e. In these areas, the Ti and O profiles clearly show an oxygen enrichment where the defects are present, i.e., at the interface and at about ca. 5 nm deeper from it. In those data, the EELS has a higher energy resolution, only ranging from Ti-L to O-K, which allows for the quantification of the Ti/O ratio and the amount of Ti^{4+}. The Ti^{4+} profile plotted in the top panel of Figure 4f is also composed of a small plateau near the interface and a decay over 5 nm.

For comparison, the expected number of holes due to a Ti/O deviation from the nominal value of 1/3 is calculated (see Figure 4f, bottom panel). This estimation considers that each interstitial oxygen injects two holes into the Ti-d orbital. When integrating the expected number of holes, they are too few to quantitatively match the amount of Ti^{4+} measured by EELS. In this case, it is estimated from the top panel of Figure 4f that the Ti^{4+} concentration averaged over the last five nanometers is approximately 0.55, while the average number of expected holes (bottom panel of Figure 4f) is ≈0.30. Furthermore, the Ti^{4+} profile obtained by EELS does not match the spatial defect distribution and the corresponding expected holes. This indicates that the charges

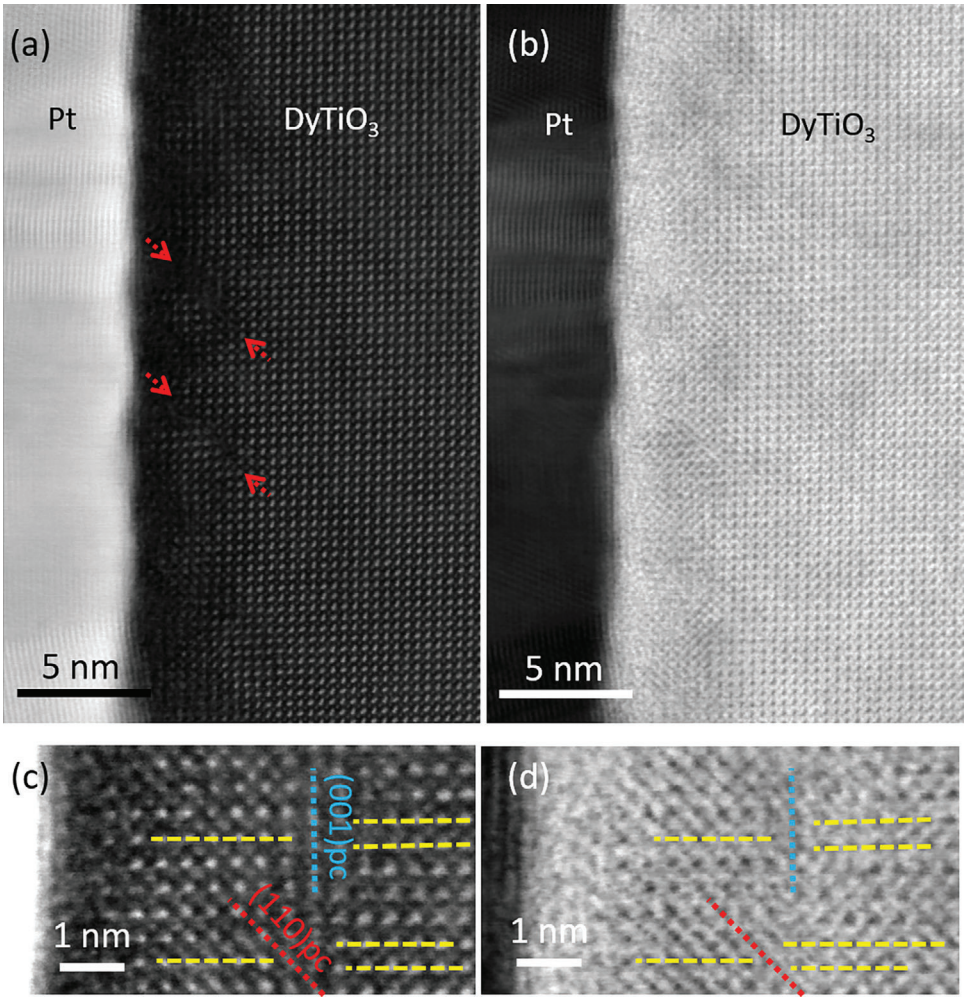

Figure 3. a,b) HAADF and BF STEM images of the top part of the DTO films. The arrows indicate {110}pc defect lines. They often occur with periodicity of ca. 5nm. c,d) Zoomed HAADF and BF STEM images nearby the defects. These images are from the thinnest part of the STEM lamella resulting in a better visualisation of the defects.

are spatially redistributed away from the defects and closer to the interface.

Figure 4g displays the EELS measurement across a relatively extended $(110)_{pc}$-type defect. The chemical maps indicate that this defect can also exhibit cation imbalance, evidenced by an increased concentration of Dy along the defect planes. Such cationic imbalance might contribute to the presence of missing holes. Recently, a new type of cationic defect has been identified in $NdTiO_3$ perovskite, involving the ordered removal of entire lines of Ti-O atoms around octahedral lines, resulting in a central octahedral line with Ti^{4+} and localized Nd enrichment.[35] Another notable structure is La_2RuO_5, as reported by Boullay et al.,[36] which features planes of perovskite cut along the $(110)_{pc}$ similar to the LP $A_nB_nO_{(3n+2)}$ with $n = 2$. Between these planes, $(AO)_2$ atoms are intercalated, potentially forming a $(DyO)_2(Dy_2Ti_2O_8)$ structure in this case, accounting for oxygen overstochiometry and cationic imbalance along $(110)_{pc}$ planes. Figure S2b,c (Supporting Information) presents these various models. The Dy/Ti modulation observed in Figure 4g is more extensive than a single vacancy line or plane and might correspond to two defective cationic planes (also see Figure S3, Supporting Information). Better alignment with these experimental observations is achieved with ab-initio relaxed structural models where a series of Ti-O and Ti vacancy planes have been removed along $(110)_{pc}$ planes (Figure S2e,f, Supporting Information). This confirms that the observed defects could be a combination of cationic vacancies and oxygen interstitials along $(110)_{pc}$ planes (Figure S3, Supporting Information). These types of defects are unevenly distributed within the top DTO layer and, being based on Ti^{3+}- or $(Ti\text{-}O)^{+}$- vacancies, they lead to hole doping. A single neutral Ti vacancy in DTO injects three holes per Ti/Dy deviation, while mixtures of Ti^{3+}- and $(Ti\text{-}O)^{+}$- vacancies result in fewer holes per Ti/Dy off-stoichiometry. To estimate the number of holes due to the cation mismatch, a conservative assumption is made, with every Ti/Dy ratio below 1 contributing 1.5 holes. Figure 4c shows a typical result of the expected Ti^{4+} profiles due to interstitial oxygens and Ti/Dy imbalance ratio. The additional holes from cationic imbalance are more prevalent near the top interface, corresponding with the chemical profile. Although the total number of holes is slightly lower than what EELS measurements indicate,

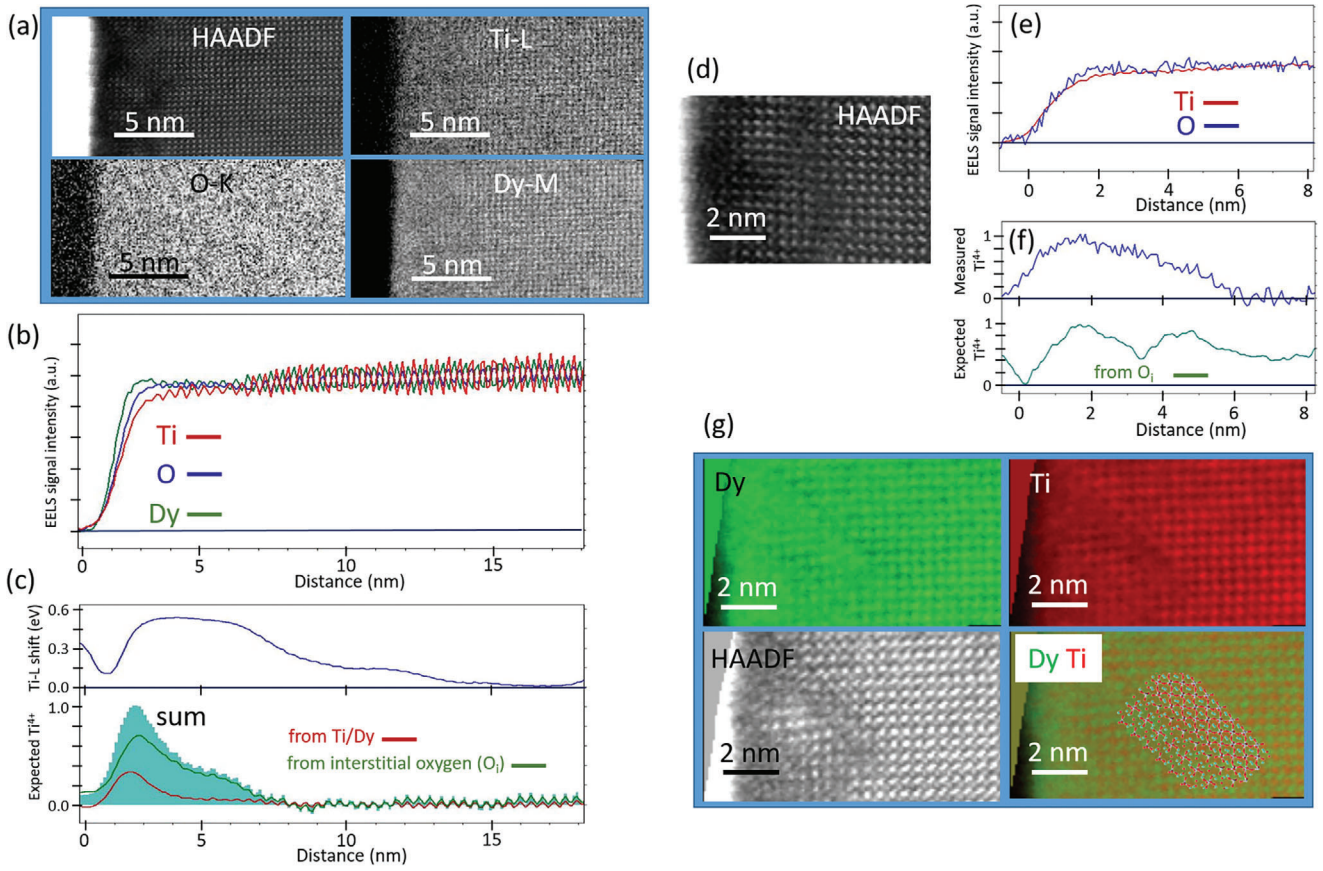

Figure 4. a–c) STEM-EELS analysis across the DTO film. The maps and profiles are respectively visible in (a) and (b). A rough estimation of the Ti valence changes have been done in c) by measuring the Ti-L energy shift. It is compared with the expected Ti^{4+} as calculated from the presence of interstitial oxygens (3 holes per O_i) and a Ti/Dy <1 (1.5 hole per Ti/Dy misbalance). The sum of both contributions are in the cyan plain curve. (d,e,f) STEM-EELS analysis across an area with marked defective areas at ca. −5 nm and near the interface as seen in HAADF STEM (d). The Ti and O profiles are in (e) and can be compared to the Ti^{4+} content obtained by fitting spectra as in Figure 2. The expected Ti^{4+} profiles considering that every interstitial oxygens gives three holes in the Ti-d orbital are also visible in the lower part of (f). g) STEM-EELS and HAADF maps of an extended (110)-type defect showing a strong Ti/Dy reduction. The Dy-M and Ti-L EELS maps are respectively green and red. A composite Dy-Ti colored map with an atomic model with 2 planes of Ti-O vacancies is superimposed (see Figure S3, Supporting Information, for detail).

the discrepancy might be due to uncertainties in the hole compensation process (Figure 4c). Nonetheless, the combination of interstitial oxygens and cationic imbalance explains the high concentration of Ti^{4+} near the top interface.

Interestingly, the STEM-EELS measurement of the Ti^{4+} distribution has shown that the hole profiles are very similar throughout the samples. They exhibit a small plateau at the interface followed by a rapid decay. On the other hand, the structural defects are spatially heterogeneously distributed, often showing a weak spatial correlation to the hole profiles. This lack of correlation is particularly evident when defects are present ≈5 nm from the interface, while the Ti^{4+} content is only weakly present at this depth (Figure 4f). As a result, the well-crystallized regions between the defects can exhibit a strong Ti^{4+} contribution concomitant with a perovskite structure. This explains why the ferromagnetic properties are depressed in thin films of $DyTiO_3$, while no evidence of superstructures or secondary phases was reported by bulk-sensitive techniques.[18] The similarity of the EELS Ti^{4+} profiles throughout the sample suggests that the hole spatial distribution is governed by the electrostatic potential well near the interface, with most of the holes being concentrated there. Similar features have been reported in 2D electron gases present in oxide thin-film interfaces as seen in the case of the $LaAlO_3$-$SrTiO_3$ interface.[37] Electrons occur from donor states, oxygen vacancies being the most common structural defects for that, and the charges being subsequently transferred to the interface by the building-up of a confining potential. In the case of $SrTiO_3$, observations for different interfaces are consistent with a rather general defect-assisted feeding of such 2D gases, thus packed near the interface by the potential well.[38]

3. Conclusion

Epitaxial perovskite $DyTiO_3$ thin films, like other perovskite rare-earth titanates $RTiO_3$, display a Ti^{4+}-rich layer over several nanometers near their surfaces and interfaces, with no secondary long-range ordered phases present. Our STEM-EELS experiments demonstrate that this intriguing and pronounced valence evolution is related to a combination of short-range ordered interstitial oxygen planes and a Ti-Dy cationic imbalance.

Both defects synergistically contribute to enough hole doping for a complete transition toward Ti^{4+} over a few unit cells from the surface, while a structure primarily of the perovskite type is maintained. The presence of interstitial oxygen and a Ti-Dy cationic imbalance can be explained in relation to previously reported phases near LP perovskite structures, such as the local presence of defects of $(DyO)_2(Dy_2Ti_2O_8)$ type, or by combining $(110)_{pc}$ planes of Ti-O and Ti vacancies, as demonstrated by ab-initio methods.

4. Experimental Section

The samples were grown on (001)-oriented $LaAlO_3$ (LAO) substrates (from CrysTec GmbH). A polycrystalline target (PiKem) consisting of a mixture of Dy_2O_3, TiO_2, and $Dy_2Ti_2O_7$ with an overall 1:1 Dy:Ti ratio was ablated by a Coherent Compact KrF (248 nm) excimer laser at a repetition rate of 2 Hz and with a fluence of 2 J cm^{-2}. The deposition has been done at a substrate temperature of 900 °C and a pressure of 4×10^{-7} mbar of O_2. The substrate-to-target distance was set to 4.5 cm. After deposition, the samples were cooled in the same growth atmosphere at 50 °C min^{-1}.[17,19]

Monochromatic STEM-EELS experiments were done on a Nion Hermes microscope with a CMOS camera as an EELS detector. Non-monochromatic STEM-EELS were done on a Nion USTEM microscope with a MerlinEM hybrid detector to collect the EELS spectra. All STEM experiments were done at 100 keV.

Ab initio relaxation of defective structures were done using Quantum Espresso.[23] Ionic convergence threshold on forces was 10^{-3} (a.u) and cell pressure threshold was 10^{-1} kbar, all coupled with a Broyden–Fletcher–Goldfarb–Shanno minimization algorithm. The exchange and correlation function was in the generalized gradient approximation in the Perdew–Burke–Ernzenhof parametrization. In accordance, the used pseudopotentials are "Dy.pbe-spdn-rrkjus_psl.1.0.0.UPF", "O.pbe-n-rrkjus_psl.1.0.0.UPF," and "Ti.pbe-spn-rrkjus_psl.1.0.0.UPF" (from http://www.quantum-espresso.org) with a wavefunction energy cut-off of 60 Ry and a charge density energy cut-off of 575 Ry.

Supporting Information

Supporting Information is available from the Wiley Online Library or from the author.

Acknowledgements

Nion CHROMATEM at LPS-Orsay and the FIB at C2N, University of Paris-Saclay were accessed in the TEMPOS project framework (ANR 10-EQPX-0050).

Conflict of Interest

The authors declare no conflict of interest.

Data Availability Statement

The data that support the findings of this study are available from the corresponding author upon reasonable request.

Keywords

electron energy loss spectroscopy, interface, magnetic oxides, Mott insulators, perovskite, scanning transmission electron microscope, surface

Received: June 3, 2024
Revised: July 8, 2024
Published online:

[1] H. Holzapfel, J. Sieler, *Z Anorg Allg Chem.* **1966**, *343*, 174.
[2] G. J. McCarthy, W. B. White, R. Roy, *Mater. Res. Bull.* **1969**, *4*, 251.
[3] P. Ganguly, O. Parkash, C. N. R. Rao, *Phys. Stat. Sol.* **1976**, *36*, 669.
[4] J. Zaanen, G. A. Sawatzky, J. W. Allen, *Phys. Rev. Lett.* **1985**, *55*, 418.
[5] A. E. Bocquet, T. Mizokawa, T. Saitoh, H. Namatame, A. Fujimori, *Phys. Rev. B.* **1992**, *46*, 3771.
[6] M. Mochizuki, M. Imada, *New J Phys.* **2004**, *6*, 154 .
[7] J. Varignon, M. N. Grisolia, D. Preziosi, P. Ghosez, M. Bibes, *Phys. Rev. B.* **2017**, *96*, 235106.
[8] J. E. Greedan, *J. Less Common Metals* **1985**, *111*, 335.
[9] C. W. Turner, M. F. Collins, J. E. Greedan, *J. Magn. Magn. Mater.* **1981**, *23*, 265.
[10] H. D. Zhou, J. B. Goodenough, *J. Phys.: Condens. Matter* **2005**, *17*, 7395 .
[11] T. Katsufuji, Y. Taguchi, Y. Tokura, *Phys. Rev. B.* **1997**, *56*, 10145.
[12] M. Heinrich, H.-A. Krug Von Nidda, V. Fritsch, A. Loidl, *Phys. Rev. B.* **2001**, *63*, 193103.
[13] S. Hameed, J. Joe, D. M. Gautreau, J. W. Freeland, T. Birol, M. Greven, *Phys. Rev. B.* **2021**, *104*, 045112.
[14] C. Ulrich, G. Ghiringhelli, A. Piazzalunga, L. Braicovich, N. B. Brookes, H. Roth, T. Lorenz, B. Keimer, *Phys. Rev. B.* **2008**, *77*, 113102.
[15] S. Hameed, S. El-Khatib, K. P. Olson, B. Yu, T. J. Williams, T. Hong, Q. Sheng, K. Yamakawa, J. Zang, Y. J. Uemura, G. Q. Zhao, C. Q. Jin, L. Fu, Y. Gu, F. Ning, Y. Cai, K. M. Kojima, J. W. Freeland, M. Matsuda, C. Leighton, M. Greven, *Phys. Rev. B.* **2021**, *104*, 024410.
[16] M. N. Grisolia, F. Y. Bruno, D. Sando, H. J. Zhao, E. Jacquet, X. M. Chen, L. Bellaiche, A. Barthélémy, M. Bibes, *Appl. Phys. Lett.* **2014**, *105*, 172402.
[17] R. Aeschlimann, M. N. Grisolia, G. Sanchez-Santolino, J. Varignon, F. Choueikani, R. Mattana, V. Garcia, S. Fusil, T. Fröhlich, M. Braden, B. Delley, M. Varela, P. Ohresser, J. Santamaria, A. Barthélémy, C. Piamonteze, M. Bibes, *Phys Rev.* **2021**, *5*, 014407.
[18] P. Scheiderer, M. Schmitt, J. Gabel, M. Zapf, M. Stübinger, P. Schütz, L. Dudy, C. Schlueter, T.-L. Lee, M. Sing, R. Claessen, *Adv. Mater.* **2018**, *30*, 1706708.
[19] R. Aeschlimann, D. Preziosi, P. Scheiderer, M. Sing, S. Valencia, J. Santamaria, C. Luo, H. Ryll, F. Radu, R. Claessen, C. Piamonteze, M. Bibes, *Adv. Mater.* **2018**, *30*, 1707489.
[20] H. Chen, C. A. Marianetti, A. J. Millis, *Phys. Rev. Lett.* **2013**, *111*, 116403.
[21] M. N. Grisolia, J. Varignon, G. Sanchez-Santolino, A. Arora, S. Valencia, M. Varela, R. Abrudan, E. Weschke, E. Schierle, J. E. Rault, J.-P. Rueff, A. Barthélémy, J. Santamaria, M. Bibes, *Nat. Phys.* **2016**, *12*, 484.
[22] G. Araizi-Kanoutas, J. Geessinck, N. Gauquelin, S. Smit, X. H. Verbeek, S. K. Mishra, P. Bencok, C. Schlueter, T.-L. Lee, D. Krishnan, J. Fatermans, J.o Verbeeck, G. Rijnders, G. Koster, M. S. Golden, *Phys. Rev.* **2020**, *4*, 026001.
[23] P. Giannozzi, S. Baroni, N. Bonini, M. Calandra, R. Car, C. Cavazzoni, D. Ceresoli, G. L. Chiarotti, M. Cococcioni, I. Dabo, A. Dal Corso, S. de Gironcoli, S. Fabris, G. Fratesi, R. Gebauer, U. Gerstmann, C. Gougoussis, A. Kokalj, M. Lazzeri, L. Martin-Samos, N. Marzari, F. Mauri, R. Mazzarello, S. Paolini, A. Pasquarello, L. Paulatto, C. Sbraccia, S. Scandolo, G. Sclauzero, A. P. Seitsonen, et al., *J. Phys.: Condens. Matter* **2009**, *21*, 395502.
[24] M. Salluzzo, J. C. Cezar, N. B. Brookes, V. Bisogni, G. M. De Luca, C. Richter, S. Thiel, J. Mannhart, M. Huijben, A. Brinkman, G. Rijnders, G. Ghiringhelli, *Phys. Rev. Lett.* **2009**, *102*, 166804.

[25] S. Mallik, G. C. Ménard, G. Saïz, I. Gilmutdinov, D. Vignolles, C. Proust, A. Gloter, N. Bergeal, M. Gabay, M. Bibes, *Nano Lett.* **2022**, *22*, 65.
[26] M. Haruta, T. Nemoto, H. Kurata, *Appl. Phys. Lett.* **2021**, *119*, 232901.
[27] S. Polisetty, J. Zhou, J. Karthik, A. R. Damodaran, D. Chen, A. Scholl, L. W. Martin, M. Holcomb, *J. Phys.: Condens. Matter* **2012**, *24*, 245902.
[28] W. Zhang, Q. Feng, E. Hosono, D. Asakura, J. Miyawaki, Y. Harada, *ACS Omega* **2020**, *5*, 22800.
[29] A. Pal, S. Ghosh, S. Kumar, E. F. Schwier, M. Sawada, K. Shimada, M. Gupta, D. M. Phase, A. K. Ghosh, S. Chatterjee, *J. Magn. Magn. Mater.* **2019**, *476*, 7.
[30] E. R. Aluri, A. P. Grosvenor, *J. Phys. Chem. Solids* **2013**, *74*, 830.
[31] D. Pravarthana, O. I. Lebedev, A. David, A. Fouchet, M. Trassin, G. S. Rohrer, P. A. Salvador, W. Prellier, *RSC Adv.* **2019**, *9*, 19895.
[32] F. Lichtenberg, A. Herrnberger, K. Wiedenmann, *Prog. Solid State Chem.* **2008**, *36*, 253.
[33] H. W. Schmalle, T. Williams, A. Reller, A. Linden, J. G. Bednorz, *Acta Cryst. B.* **1993**, *49*, 235.
[34] A. Ohtomo, D. A. Muller, J. L. Grazul, H. Y. Hwang, *Appl. Phys. Lett.* **2002**, *80*, 3922.
[35] J. S. Jeong, M. Topsakal, P. Xu, B. Jalan, R. M. Wentzcovitch, K. A. Mkhoyan, *Nano Lett.* **2016**, *16*, 6816.
[36] P. Boullay, D. Mercurio, A. Bencan, A. Meden, G. Drazic, M. Kosec, *J. Solid State Chem.* **2003**, *170*, 294.
[37] M. Basletic, J.-L. Maurice, C. Carrétéro, G. Herranz, O. Copie, M. Bibes, É. Jacquet, K. Bouzehouane, S. Fusil, A. Barthélémy, *Nat. Mater.* **2008**, *7*, 621.
[38] U. Treske, N. Heming, M. Knupfer, B. Büchner, E. Di Gennaro, A. Khare, U. Scotti Di Uccio, F. Miletto Granozio, S. Krause, A. Koitzsch, *Sci. Rep.* **2015**, *5*, 14506.